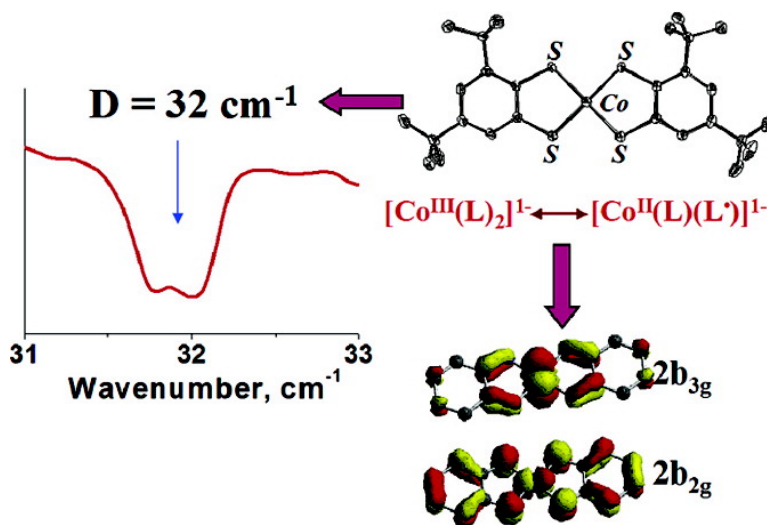


The Electronic Structure of the Isoelectronic, Square-Planar Complexes $[\text{Fe}(\text{L})]$ and $[\text{Co}(\text{L})]$ (L and $(\text{L})^-$ = Benzene-1,2-dithiolates): An Experimental and Density Functional Theoretical Study

Kallol Ray, Ameerunisha Begum, Thomas Weyhermüller, Stergios Piligkos, Joris van Slageren, Frank Neese, and Karl Wieghardt

J. Am. Chem. Soc., **2005**, 127 (12), 4403-4415 • DOI: 10.1021/ja042803i • Publication Date (Web): 08 March 2005

Downloaded from <http://pubs.acs.org> on March 24, 2009



More About This Article

Additional resources and features associated with this article are available within the HTML version:

- Supporting Information
- Links to the 18 articles that cite this article, as of the time of this article download
- Access to high resolution figures
- Links to articles and content related to this article
- Copyright permission to reproduce figures and/or text from this article

[View the Full Text HTML](#)

The Electronic Structure of the Isoelectronic, Square-Planar Complexes $[\text{Fe}^{\text{II}}(\text{L})_2]^{2-}$ and $[\text{Co}^{\text{III}}(\text{L}^{\text{Bu}})_2]^-$ (L^{2-} and $(\text{L}^{\text{Bu}})^{2-} = \text{Benzene-1,2-dithiolates}$): An Experimental and Density Functional Theoretical Study

Kallol Ray,[†] Ameerunisha Begum,[†] Thomas Weyhermüller,[†] Stergios Piligkos,[†] Joris van Slageren,[‡] Frank Neese,^{*,†} and Karl Wieghardt^{*,†}

Contribution from the Max-Planck-Institut für Bioanorganische Chemie, Stiftstrasse 34-36, D-45470 Mülheim an der Ruhr, Germany, and 1.Physikalisches Institut, Universität Stuttgart, Pfaffenwaldring 57, D-70550 Stuttgart, Germany

Received November 30, 2004; E-mail: neese@mpi-muelheim.mpg.de; wieghardt@mpi-muelheim.mpg.de

Abstract: The electronic structures of two formally isoelectronic transition-metal dithiolato complexes $[\text{Fe}(\text{L})_2]^{2-}$ (**1**) and $[\text{Co}(\text{L}^{\text{Bu}})_2]^{1-}$ (**2**) both possessing a spin triplet ground state ($S_t = 1$) have been investigated by various spectroscopic and density functional methods; $\text{H}_2\text{L}^{\text{Bu}}$ represents the pro-ligand 3,5-di-*tert*-butylbenzene-1,2-dithiol and H_2L is the corresponding unsubstituted benzene-1,2-dithiol. An axial zero-field splitting (D) of $+32 \text{ cm}^{-1}$ for **2** has been measured independently by SQUID magnetometry, far-infrared absorption, and variable-temperature and variable-field (VTVH) magnetic circular dichroism spectroscopies. A similar D value of $+28 \text{ cm}^{-1}$ is obtained for **1** on the basis of VTVH SQUID measurements. The absorption spectra of **1** and **2** are found, however, to be very different. Complex **1** is light yellow in color with no intense transition in the visible region, whereas **2** is deep blue. DFT calculations establish that the electronic structures of the $[\text{Fe}(\text{L})_2]^{2-}$ and $[\text{Co}(\text{L})_2]^{1-}$ anions are very different and explain the observed differences in their absorption spectra. On the basis of these spectroscopic and theoretical analyses, **1** is best described as containing an intermediate spin Fe(II) ion, whereas for the corresponding cobalt complex, oxidation states describing a d^6 (Co^{III}) or d^7 (Co^{II}) electron configuration cannot be unambiguously assigned. The physical origin of the large zero-field splitting in both **1** and **2** is found to be due to the presence of low-energy spin-conserved $d-d$ excitations which lead to a large D_{zz} through efficient spin-orbit coupling. Differential covalency effects appear to be of limited importance for this property.

Introduction

In 1984, Sellmann et al.¹ synthesized the yellow complex $(\text{AsPh}_4)_2[\text{Fe}^{\text{II}}(\text{S}_2\text{C}_6\text{H}_4)_2]$ and showed by room-temperature X-ray crystallography that the salt consists of well-separated tetraphenylarsonium cations and square-planar bis(benzene-1,2-dithiolato)iron(II) dianions (2:1). The complex was shown to possess an effective magnetic moment of $3.55 \mu_B$ at 295 K, which is possibly indicative of an $S = 1$ ground state (d^6). Later the zero-field Mössbauer spectrum at 85 K was also reported:² $\delta = 0.435 \text{ mm/s}$, $\Delta E_q = 1.161 \text{ mm/s}$. The oxidation level of the benzene-1,2-dithiolato ligands as closed-shell aromatic dianions was clearly established by the observed long C–S bonds at $1.76 \pm 0.02 \text{ \AA}$ (the error corresponds to three times the estimated standard deviation, 3σ) and six nearly equidistant aromatic C–C bond lengths. Since the errors are rather large, we decided to reinvestigate the structure at cryogenic temper-

ature (100 K) and to study its variable-temperature magnetism and electronic spectra. For this purpose we synthesized the new, yellow, crystalline salt $[\text{N}(\text{C}_2\text{H}_5)_3\text{H}]_2[\text{Fe}(\text{S}_2\text{C}_6\text{H}_4)_2]$ (**1**).

The corresponding isoelectronic monoanion $[\text{Co}^{\text{III}}(\text{S}_2\text{C}_6\text{H}_4)_2]^-$ and its toluene-3,4-dithiolato, $(\text{tdt})^{2-}$, analogue $[\text{Co}(\text{tdt})_2]^-$ have been the archetypical complexes for square-planar coordination since their discovery as early as 1963^{3–5} and subsequent structural characterization.^{6,7} They are deep blue complexes with an $S = 1$ ground state.⁸ The possibility to describe the electronic structure as singlet with an energetically low-lying triplet excited state has also been considered.⁹ On the other hand, van der Put et al.⁸ conclusively showed experimentally that these monoanions possess an $S = 1$ ground state with a large zero-field

- (3) Gray, H. B.; Billig, E. *J. Am. Chem. Soc.* **1963**, *85*, 2019.
- (4) Williams, R.; Billig, E.; Waters, J. H.; Gray, H. B. *J. Am. Chem. Soc.* **1966**, *88*, 43.
- (5) Baker-Hawkes, M. J.; Billig, E.; Gray, H. B. *J. Am. Chem. Soc.* **1966**, *88*, 4870.
- (6) Eisenberg, R.; Dori, Z.; Gray, H. B.; Ibers, J. A. *Inorg. Chem.* **1968**, *7*, 741.
- (7) Baker-Hawkes, M. J.; Dori, Z.; Eisenberg, R.; Gray, H. B. *J. Am. Chem. Soc.* **1968**, *90*, 4253.
- (8) van der Put, P. J.; Schilperoord, A. A. *Inorg. Chem.* **1974**, *13*, 2476.
- (9) Ollis, C. R.; Jeter, D. Y.; Hatfield, W. E. *J. Am. Chem. Soc.* **1971**, *93*, 547.

[†] Max-Planck-Institut für Bioanorganische Chemie.

[‡] Universität Stuttgart.

- (1) (a) Sellmann, D.; Kleine-Kleffmann, U.; Zapf, L.; Huttner, G.; Zsolnai, L. *J. Organomet. Chem.* **1984**, *263*, 321. (b) For a series of reviews in dithiolene chemistry, see: *Prog. Inorg. Chem.* **2003**, *52*, 55.
- (2) Sellmann, D.; Geck, M.; Moll, M. *J. Am. Chem. Soc.* **1991**, *113*, 5259.

splitting (ZFS) of $+35\text{ cm}^{-1}$, the origin of which remained unclear. Later, Sawyer et al.¹⁰ suggested an electronic structure $[\text{Co}^{\text{II}}(\text{L}^*)(\text{L})]^{-}$ involving Co(II) ($S_{\text{Co}} = 3/2$) and an antiferromagnetically coupled ligand π -radical $(\text{L}^*)^{1-}$.

All previous structural characterizations of such monoanions have been plagued by crystallographic problems (e.g., static disorder) which prevented the accurate determination of C–S and C–C bond lengths with only small estimated standard deviations of maximally $\pm 0.003\text{ \AA}$ ($\sigma = 0.003\text{ \AA}$). The structure of the diamagnetic monoanionic adduct $[\text{Co}^{\text{III}}(\text{S}_2\text{C}_6\text{H}_4)_2(\text{P}^{\text{nBu}})_3]^{-}$ $[\text{PH}^{\text{nBu}}_3]$ has also been determined,¹¹ but again the standard deviations are rather large. The experimental determination of the oxidation level of these benzene-1,2-dithiolate ligands has never been unequivocal.

In this work, we employed Sellmann's ligand^{12,13} 3,5-di-*tert*-butylbenzene-1,2-dithiol, $\text{H}_2[\text{L}^{\text{Bu}}]$. The following complexes have been synthesized: yellow $[\text{HN}(\text{C}_2\text{H}_5)_3]_2[\text{Fe}^{\text{II}}(\text{L})_2]$ (**1**) where L^{2-} is the unsubstituted benzene-1,2-dithiolate ligand and its analogue $[\text{N}(\text{n-Bu})_4]_2[\text{Fe}^{\text{II}}(\text{L})_2]$ (**1a**) and the deep blue complexes $[\text{N}(\text{n-Bu})_4][\text{Co}^{\text{III}}(\text{L}^{\text{Bu}})_2]$ (**2**) and $[\text{As}(\text{CH}_3)\text{Ph}_3][\text{Co}^{\text{III}}(\text{L}^{\text{Bu}})_2]$ (**2a**). The high quality X-ray structure determinations of **1** and **2a** at 100 K are reported. Their electronic structures have been studied spectroscopically (electronic absorption, Mössbauer far-infrared, and magnetic circular dichroism (MCD) spectroscopy) and by density functional theoretical calculations. We attempt to understand the origin of the large ZFS of both triplet systems, namely $[\text{Fe}^{\text{II}}(\text{L})_2]^{2-}$ and $[\text{Co}^{\text{III}}(\text{L})_2]^{-}$, and also why the colors of the isoelectronic iron(II) and cobalt(III) complexes are so different.

Experimental Section

The ligand 3,5-di-*tert*-butylbenzene-1,2-dithiol, $\text{H}_2[\text{L}^{\text{Bu}}]$, has been prepared as described in refs 12 and 13. Benzene-1,2-dithiol, H_2L , is commercially available.

$[\text{HN}(\text{C}_2\text{H}_5)_3]_2[\text{Fe}^{\text{II}}(\text{L})_2]$ (1**).** Triethylamine (0.36 mL, 3 mmol) was added to a solution of the ligand $\text{H}_2(\text{L})$ (140 mg, 1.0 mmol) in tetrahydrofuran (5 mL) under an Ar blanketing atmosphere. A solution of $\text{FeCl}_2 \cdot 4\text{H}_2\text{O}$ (99 mg, 0.5 mmol) in degassed THF (5 mL) was slowly added to the above solution at 20 °C under anaerobic conditions in a glovebox. The resulting dark red solution was stirred for 2 h, during which time an extremely air-sensitive yellowish-brown powder of **1** precipitated. Yield: 170 mg (58%). Anal. Calcd for $\text{C}_{24}\text{H}_{40}\text{N}_2\text{S}_4\text{Fe}$: C, 53.31; H, 7.46; N, 5.18. Found: C, 53.1; H, 7.32; N, 5.05. The corresponding complex $[\text{N}(\text{n-Bu})_4]_2[\text{Fe}^{\text{II}}(\text{L})_2]$ (**1a**) has been prepared analogously by addition of $[\text{N}(\text{n-Bu})_4]\text{Br}$ for precipitation.

$[\text{N}(\text{n-Bu})_4][\text{Co}^{\text{III}}(\text{L}^{\text{Bu}})_2]$ (2**).** To a solution of the ligand $\text{H}_2(\text{L}^{\text{Bu}})$ (650 mg, 2.6 mmol) in absolute ethanol (20 mL) was added potassium metal (240 mg, 6 mmol) under an Ar blanketing atmosphere. To this solution was added solid anhydrous CoCl_2 (169 mg, 1.3 mmol) at 20 °C. The greenish solution was then exposed to air, whereupon a color change to deep blue was observed. Addition of $[\text{N}(\text{n-Bu})_4]\text{Br}$ (420 mg, 1.3 mmol) initiated the precipitation of a deep blue powder, which was redissolved in dry CH_2Cl_2 (200 mL). After filtration the solvent volume was reduced to 20 mL by evaporation of the solvent under reduced pressure. Keeping the solution for $\sim 1\text{ h}$ under a continuous flow of

Table 1. Crystallographic Data for **1** and **2a**

	1	2a
chem formula	$\text{C}_{24}\text{H}_{40}\text{FeN}_2\text{S}_4$	$\text{C}_{47}\text{H}_{58}\text{AsCoS}_4$
fw	540.67	885.02
space group	$P2_1/n$, No. 14	$P2_1/c$, No. 14
<i>a</i> , Å	7.3798(6)	11.4045(6)
<i>b</i> , Å	13.4220(8)	13.0763(6)
<i>c</i> , Å	13.5820(9)	31.143(2)
β , deg	100.51(1)	93.20(1)
<i>V</i> , Å ³	1322.7(2)	11992.6(6)
<i>Z</i>	2	4
<i>T</i> , K	100(2)	100(2)
ρ calcd, g cm ⁻³	1.357	1.268
reflms collected/ $2\Theta_{\text{max}}$	13959/66.3	35660/55.0
unique reflms/ $I > 2\sigma(I)$	5023/4128	10639/7205
No. of params/restr.	145/0	491/0
μ (Mo K α), cm ⁻¹	9.01	12.88
R1 ^a /GOF ^b	0.0331/1.035	0.0450/1.009
wR2 ^c ($I > 2\sigma(I)$)	0.0739	0.0790
resid. density, e Å ⁻³	+0.48/−0.50	+0.54/−0.46

^a Observation criterion: $I > 2\sigma(I)$. $R1 = \sum ||F_o| - |F_c|| / \sum |F_o|$. ^b GOF = $\{\sum [w(F_o^2 - F_c^2)]^2 / (n - p)\}^{1/2}$. ^c wR2 = $\{\sum [w(F_o^2 - F_c^2)]^2 / \sum [w(F_o^2)]^2\}^{1/2}$ where $w = 1/\sigma^2(F_o^2) + (aP)^2 + bP$, $P = (F_o^2 + 2F_c^2)/3$.

Ar resulted in the separation of shining, deep blue crystals. Yield: 1.42 g (73%). Anal. Calcd for $\text{C}_{44}\text{H}_{76}\text{S}_4\text{NCo}$: C, 65.59; H, 9.44; N, 1.74; S, 15.98; Co, 7.33. Found: C, 65.40; H, 9.42; N, 1.75; S, 16.01; Co, 7.88. Electrospray mass spectrum (CH_2Cl_2 solution) positive and negative ion mode: $m/z = 563$ $\{\text{Co}(\text{L}^{\text{Bu}})_2\}^+$; 242.3 $\{\text{N}(\text{n-Bu})_4\}^+$.

By using $[\text{AsMePh}_3]\text{I}$ in the above reaction instead of $[\text{N}(\text{n-Bu})_4]\text{Br}$, we isolated the blue complex $[\text{AsMePh}_3][\text{Co}^{\text{III}}(\text{L}^{\text{Bu}})_2]$ (**2a**). Single crystals suitable for X-ray crystallography were obtained by recrystallization of this material from a $\text{CH}_2\text{Cl}_2/\text{C}_2\text{H}_5\text{OH}$ mixture (1:1).

X-ray Crystallographic Data Collection and Refinement of the Structures. A dark orange single crystal of **1** and a dark blue crystal of **2a** were coated with perfluoropolyether, picked up with a glass fiber, and mounted in the nitrogen cold stream of the diffractometer. Intensity data were collected at 100 K using a Nonius Kappa CCD diffractometer equipped with a Mo-target rotating-anode X-ray source and a graphite monochromator (Mo K α , $\lambda = 0.71073\text{ \AA}$). Final cell constants were obtained from a least-squares fit of a subset of several thousand intense reflections. Crystal faces of **2a** were determined, and the corresponding intensity data were corrected for absorption using the Gaussian-type routine embedded in XPREP.¹⁴ The data set of **1** was left uncorrected. Crystallographic data of the compounds are listed in Table 1. The Siemens SHELXTL¹⁴ software package was used for solution and artwork of the structure, and SHELXL97¹⁵ was used for the refinement. The structures were readily solved by direct methods and subsequent difference Fourier techniques. All non-hydrogen atoms were refined anisotropically, and hydrogen atoms were placed at calculated positions and refined as riding atoms with isotropic displacement parameters.

Physical Measurements. MCD Spectroscopy. Magnetic circular dichroism spectra were obtained on a home-built instrument consisting of a JASCO J-715 spectropolarimeter and an Oxford Instruments Spectromag magnetocryostat which is capable of generating magnetic fields up to 11T. Spectra were taken for samples dissolved in butyronitrile, which resulted in high quality glasses suitable for optical spectroscopy at low temperatures. Experiments on solid samples were also conducted but led to less reliable spectra due to strong scattering contributions. Simultaneous Gaussian resolution of absorption and MCD spectra was performed using Peakfit 4. C/D ratios were calculated by:

(10) Sawyer, D. T.; Srivatsa, G. S.; Bodini, M. E.; Schaefer, W. P.; Wing, R. M. *J. Am. Chem. Soc.* **1986**, *108*, 936.

(11) Kang, B.; Peng, J.; Hong, M.; Wu, D.; Chen, X.; Weng, L.; Lei, X.; Liu, H. *J. Chem. Soc., Dalton Trans.* **1991**, 2897.

(12) Sellmann, D.; Freyberger, G.; Eberlein, R.; Böhlen, E.; Huttner, G.; Zsolnai, L. *J. Organomet. Chem.* **1987**, *323*, 21.

(13) Sellmann, D.; Käppler, O. *Z. Naturforsch.* **1987**, *42b*, 1291.

(14) SHELXTL, version 5; Siemens Analytical X-ray Instruments Inc.: Madison, WI, 1994.

(15) Sheldrick, G. M. SHELXL97; University of Göttingen: Göttingen, Germany, 1997.

$$\frac{C}{D} = \frac{k_{\text{B}}T}{\mu_{\text{B}}B} \frac{\int \frac{\Delta\epsilon(\nu)}{\nu} d\nu}{\int \frac{\epsilon(\nu)}{\nu} d\nu}$$

for spectra taken in the linear region of the MCD C-term response (32 K and 5 T). Simulations and fittings of variable-temperature and variable-field (VTVH) MCD data were done according to the earlier developed general MCD theory and the associated fitting program.¹⁶

Far-Infrared Spectroscopy. The measurements were performed on a Bruker IFS113v spectrometer equipped with a mercury lamp as a light source, a 50- μm Mylar beam splitter, an Infrared Labs pumped Si bolometer, and a 5-mm aperture. The sample was put into an Oxford Instruments Spectromag 4000 8 T split coil magnetic cryostat with specially enlarged Mylar windows. The spectra (typically 32 scans) were recorded on a 1-cm-diameter pressed powder pellet of the compound (160 mg) at various temperatures from 2 to 80 K and magnetic fields from 0 to 7 T.

Calculations. All calculations in this work were performed with the electronic structure program ORCA.¹⁷ As will be further discussed in the text, the geometry optimizations were carried out at the BP86 level¹⁸ of DFT. These functionals have proved in many applications their ability to reliably predict structures of transition-metal complexes. In anticipation of a forthcoming study in which analogous complexes with heavier metals are studied, we have carried out the present calculations with inclusion of scalar relativistic effects at the second-order Douglas–Kroll–Hess level (DKH2).¹⁹ In the geometry optimizations, the one-center approximation was used which eliminates DKH2 contributions to the analytic gradients. In the ZORA^{20a} context it has been shown that the one-center approximation introduces only minor errors in the final geometries.^{20b} Large uncontracted Gaussian basis sets were used at the metal center which were derived from the well-tempered basis sets of Huzinaga.²¹ For the remaining atoms, we used the all-electron polarized triple- ξ (TZVP)²² Gaussian basis sets of the Ahlrichs group but uncontracted them to allow for a distortion of the inner shell orbitals in the presence of the relativistic potential.

The property calculations at the optimized geometries were done with the B3LYP functional.²³ In this case, the same basis sets were used but the quasi-relativistic ZORA method²⁰ was used since in this formalism magnetic properties are more readily formulated.²⁴ TD-DFT calculations were carried out according to ref 25. The ZFS tensors were computed at the BP86 level using a quasi-restricted DFT-based formalism. In this method, configuration state functions of correct spin multiplicity are constructed and the contributions of the different spin channels to the **D**-tensor are computed as derived in our earlier work.²⁶ The spin–orbit coupling (SOC) operator used in this work is the recently implemented²⁷ accurate approximation to the complete mult-center mean-field spin–orbit Hamiltonian²⁸ and is expected to give

essentially the same result as the much more computationally demanding full two-electron Breit–Pauli spin–orbit operator.²⁸ Mössbauer parameters were calculated by using CP(PPP) basis sets with three additional steep functions for the iron atom.

Since the compounds studied in this work are anions, we have also carried out the calculations in solution by using the conductor-like screening model (COSMO)²⁹ as implemented in ORCA and by using CH_2Cl_2 as solvent. The effect on the predicted geometries and calculated **D**-tensors proved to be negligible, but the calculated absorption spectrum for the $[\text{Fe}(\text{L})_2]^{2-}$ species was found to be improved significantly by the COSMO method as will be described below. Natural population analysis³⁰ was done through an interface of ORCA to the gennb program version 5.0. Isocontour plots were done with Molekel³¹ and ChemBats3D.³²

Results and Discussion

Synthesis and Characterization. The reaction of the ligand benzene-1,2-dithiol, $\text{H}_2[\text{L}]$, and NEt_3 (1:2) under strictly anaerobic conditions in tetrahydrofuran with $\text{FeCl}_2 \cdot 4\text{H}_2\text{O}$ at 20 °C resulted in a dark red solution from which extremely air-sensitive yellow-brown crystals of $[\text{HN}(\text{Et})_3]_2[\text{Fe}^{\text{II}}(\text{L})_2]$ (**1**) precipitated slowly. By adding $[\text{N}(n\text{-Bu})_4]\text{Br}$ to the above solution, we isolated yellow microcrystalline $[\text{N}(n\text{-Bu})_4]_2[\text{Fe}(\text{L})_2]$ (**1a**). The corresponding $[\text{AsPh}_4]^+$ and $[\text{N}(\text{CH}_3)_4]^+$ salts have been described previously.^{1,2}

The reaction of the disodium salt of Sellmann's ligand^{12,13} 3,5-di-*tert*-butyl-1,2-benzenedithiol, $\text{H}_2(\text{L}^{\text{Bu}})$, in ethanol with CoCl_2 (2:1) under an argon atmosphere yielded a greenish solution. Exposure to air initiated a color change to deep blue. Addition of $[\text{N}(n\text{-Bu})_4]\text{Br}$ to this solution afforded deep blue crystals of $[\text{N}(n\text{-Bu})_4][\text{Co}^{\text{III}}(\text{L}^{\text{Bu}})_2]$ (**2**) in good yields. By using $[\text{As}(\text{CH}_3)_3\text{Ph}_3]\text{I}$, we obtained the salt $[\text{As}(\text{CH}_3)_3\text{Ph}_3][\text{Co}^{\text{III}}(\text{L}^{\text{Bu}})_2]$ (**2a**).

Absorption Spectra. The electronic spectrum of yellow **1** in tetrahydrofuran is shown in Figure 1 (top). Interestingly, no bands are observed in the visible region (460–1000 nm). In contrast, the spectrum of deep blue **2** (Figure 1, bottom) in CH_2Cl_2 solution displays intense charge transfer (CT) bands in the visible region (500–700 nm). These spectra will be further discussed later.

Magnetic Susceptibility. The temperature dependencies of magnetic moments of **1** and **2** are shown in Figure 2. The magnetization data $M_{\text{mol}}/Ng\beta$ versus $\beta H/kT$ of **1** and **2** have also been recorded at 1, 4, and 7 T, respectively, where M_{mol} represents the molecular magnetization, N is Avogadro's number, β is the Bohr magneton, H is the magnetic field, k is Boltzmann's constant, and T is the absolute temperature. In the range 50–298 K temperature-independent moments of $3.18 \pm 0.01 \mu_{\text{B}}$ for **1** and $2.83 \pm 0.01 \mu_{\text{B}}$ for **2** are indicative of a triplet ground state ($S = 1$) for both complexes. Below 50 K the magnetic moments drop monotonically to $\sim 0.8 \mu_{\text{B}}$ at 2 K in both cases. This temperature dependence was adequately modeled by ZFS. Thus, the following parameters gave excellent fits (Figure 2) for **1** (and in parentheses for **2**): $g_{\text{iso}} = 2.05$ (2.17), $D = +28$ (+32) cm^{-1} , $E/D = 0.1$ (0.1). Small amounts

- (16) Neese, F.; Solomon, E. I. *Inorg. Chem.* **1999**, *38*, 1847.
 (17) Neese, F. Orca- an ab initio, DFT and semiempirical electronic structure package, version 2.4, revision 16; Max-Planck Institut für Bioanorganische Chemie: Mülheim, Germany, November 2004.
 (18) (a) Becke, A. D. *J. Chem. Phys.* **1988**, *84*, 4524. (b) Perdew, J. P. *Phys. Rev. B* **1986**, *33*, 8522.
 (19) Hess, B. A.; Marian, C. M. In *Computational Molecular Spectroscopy*; Jensen, P., Bunker, P. R., Eds.; Wiley & Sons: New York, 2000; p 169ff.
 (20) (a) van Lenthe, E.; Snijders, J. G.; Baerends, E. J. *J. Chem. Phys.* **1996**, *105*, 6505. (b) van Lenthe, J. H.; Faas, S.; Snijders, J. G. *Chem. Phys. Lett.* **2000**, *328*, 107.
 (21) (a) Huzinaga, S.; Miguel, B. *Chem. Phys. Lett.* **1990**, *175*, 289. (b) Huzinaga, S.; Klobukowski, M. *Chem. Phys. Lett.* **1993**, *212*, 260.
 (22) (a) Schäfer, A.; Horn, H.; Ahlrichs, R. *J. Chem. Phys.* **1992**, *97*, 2571. (b) Schäfer, A.; Huber, C.; Ahlrichs, R. *J. Chem. Phys.* **1994**, *100*, 5289.
 (23) (a) Lee, C.; Yang, W.; Parr, R. G. *Phys. Rev. B* **1988**, *37*, 785. (b) Becke, A. D. *J. Chem. Phys.* **1993**, *98*, 5648.
 (24) van Lenthe E.; van der Avoird, A.; Wormer, P. E. *S. J. Chem. Phys.* **1998**, *108*, 4783.
 (25) Neese, F.; Olbrich, G. *Chem. Phys. Lett.* **2002**, *362*, 170.
 (26) Neese, F.; Solomon, E. I. *Inorg. Chem.* **1998**, *37*, 6568.
 (27) Neese, F. *J. Chem. Phys.* **2005**, *122*, 034107.
 (28) Hess, B. A.; Marian, C. M.; Wahlgren, U.; Gropen, O. *Chem. Phys. Lett.* **1996**, *251*, 365.

- (29) Klamt, A.; Schuurmann, G. *J. Chem. Soc., Perkin Trans.* **1993**, *2*, 793.
 (30) (a) Reed, A. E.; Weinhold, F. *J. Chem. Phys.* **1983**, *78*, 4066. (b) Reed, A. E.; Weinstock, R. B.; Weinhold, F. *J. Chem. Phys.* **1985**, *83*, 735. (c) Reed, A. E.; Curtiss, L. A.; Weinhold, F. *Chem. Rev.* **1988**, *88*, 899.
 (31) (a) Flükiger, P.; Lüthi, H. P.; Portmann, S.; Weber, J. *MOLEKEL 4.2*; Swiss Center for Scientific Computing: Manno, Switzerland, 2000–2002. (b) Portmann, S.; Lüthi, H. P. *Chimia* **2000**, *54*, 766.
 (32) *ChemBats3d*, version 6.0; <http://www.cambridgesoft.com>, 2000.

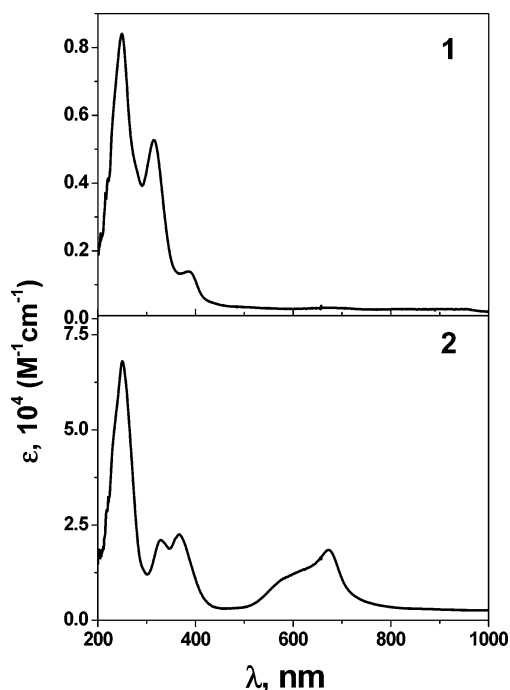


Figure 1. Electronic absorption spectra of **1** in tetrahydrofuran under an Ar blanketing atmosphere (top) and of **2** in CH_2Cl_2 (bottom).

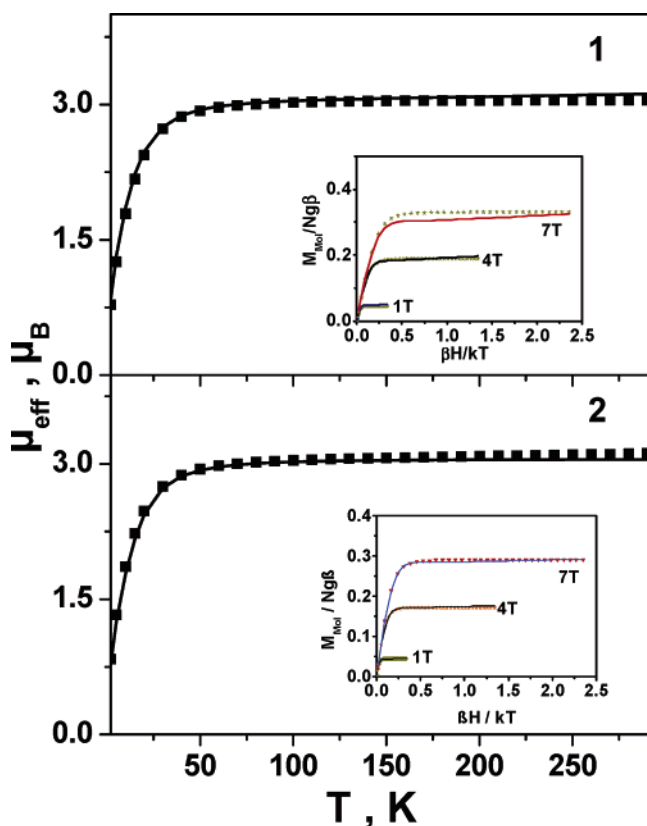


Figure 2. Temperature dependence of the magnetic moments, μ_{eff} , μ_{B} , of solid **1** (top) and **2** (bottom). The insets show magnetization data $M_{\text{mol}}/Ng\beta$ vs $\beta H/kT$. Solid lines represent best fits (for the parameters see text).

of paramagnetic impurities of 0.3% ($S = 2$) for **1** and 0.1% ($S = 3/2$) for **2** were also taken into account in the above fits. The spin-Hamiltonian (eq 1) was used:

$$\hat{H} = g\mu_{\text{B}}\mathbf{H}\mathbf{S} + D[S_z^2 - S(S+1)/3] + E[S_x^2 - S_y^2] \quad (1)$$

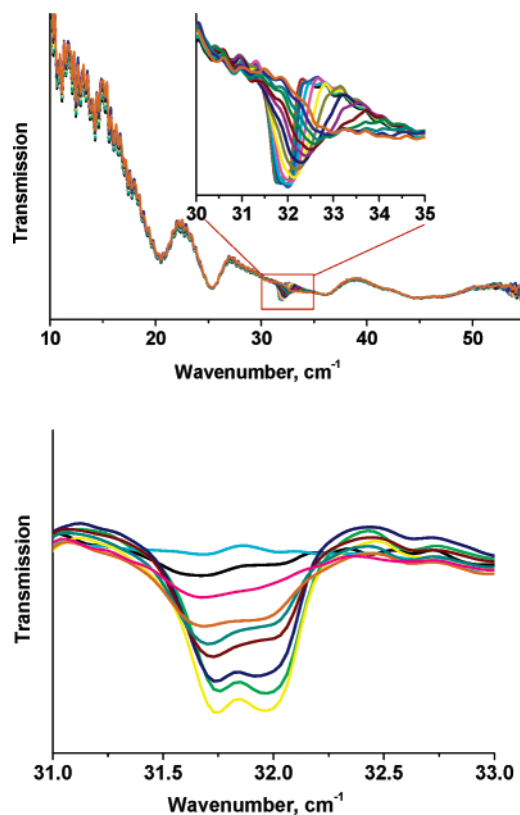


Figure 3. Far-infrared absorption spectra of **2**. Top: Spectra recorded in the range 10–50 cm^{-1} at 4.2 K and applied magnetic fields (inset) between 0 (left-hand side spectrum of inset) and 7 T (right-hand side of inset) in intervals of 0.5 T Bottom: Temperature dependence of the absorption band at 32 cm^{-1} with the maximum intensity at 4.2 K and zero intensity at 150 K.

where \mathbf{H} is the applied magnetic field, g is the g -tensor, S is the electronic spin, and D and E are parameters that describe the effects of axial and rhombic ligand fields, respectively. The signs of the ZFS parameter D of **1** and **2** shown as insets in Figure 2 have been determined from the VTVH magnetization data to be positive in both cases. We note that a fit of data in Figure 2 for **1** obtained using $D = -28 \text{ cm}^{-1}$ yields an E/D limiting value of 0.33, which is physically unreasonable for a symmetrical square-planar structure. With E/D fixed at ~ 0.1 , no satisfactory fit of the data was obtained. A similar result has been obtained for **2**.

Far Infrared Spectroscopy. The above ZFS values agree nicely with those reported for $[\text{N}(n\text{-Bu})_4][\text{Co}^{\text{III}}(\text{L}')_2]$ and in parentheses for $[\text{N}(n\text{-Bu})_4][\text{Co}^{\text{III}}(\text{L})_2]$, where L' represents toluene-3,4-dithiolate: $D = 39.4 (37.4) \text{ cm}^{-1}$; $g_{\perp} = 2.27 (2.31)$, $g_{\parallel} = 2.09 (2.19)$.⁸ As was demonstrated convincingly by van der Put and Schilperoord in 1974, the ZFS parameter can be directly measured by far-infrared spectroscopy where electronic transitions at $+34 \text{ cm}^{-1}$ have been observed for $[\text{N}(n\text{-Bu})_4][\text{Co}(\text{L})_2]$ and $[\text{N}(n\text{-Bu})_4][\text{Co}^{\text{III}}(\text{L}')_2]$, respectively, which have been assigned as the intratriplet transition between the $M_s = 0$ and $M_s = \pm 1$ components of their triplet ground states. This was based on the temperature dependence of the intensities of these bands (vanishingly small at high temperatures (298 K) and quite intense at 15 K).

Figure 3 shows the far-infrared transmission spectra of **2** in the range 10–50 cm^{-1} as a function of (a) the external magnetic field and (b) the temperature that allows us to discern between

electronic transitions on one hand and phonon bands on the other. The temperature was varied from 4.2 to 150 K, and the magnetic field between 0 and 7 T. A very sharp band with a width of $\sim 1 \text{ cm}^{-1}$ at 32 cm^{-1} is observed at zero field and 4.2 K. This band disappears completely at 150 K. Whereas all other bands remain unaffected on application of an external magnetic field, the band at 32 cm^{-1} moves to higher frequency (from 31.8 cm^{-1} at 0 T to 32.8 cm^{-1} at 7 T at 4.2 K). The ZFS parameter $D = +32 \text{ cm}^{-1}$ is thus directly obtained from the far-infrared measurements which agrees perfectly with the value obtained from the temperature-dependent magnetic susceptibility measurements.

Because of the extreme air sensitivity of the $[\text{Fe}(\text{L})_2]^{2-}$ ion, we have not been able to record the far-infrared spectrum of **1** or **1a**. It is noted that the square-planar phthalocyanine iron(II) complex possesses an $S = 1$ ground state. A ZFS parameter of $D = +64 \text{ cm}^{-1}$ at $g = 2.74$ has been established from variable-temperature magnetic susceptibility measurements.³³

Variable-Temperature Variable-Field Magnetic Circular Dichroism. The VTVH-MCD spectrum of a frozen solution of **2** in butyronitrile to be discussed together with the theoretical results below revealed the presence of temperature-dependent MCD bands throughout the investigated spectral region (1100–270 nm, *vide infra*). Consequently, all observed features are assigned to C -terms which can be used to obtain an independent measurement of the ground-state spin-Hamiltonian parameters.^{16,34}

The saturation behavior of the MCD absorption bands in the region between 12 000 and 20 000 cm^{-1} (500–830 nm) was investigated by monitoring the intensity of a given absorption band upon field and temperature variation. It has been shown¹⁶ that, in the case of randomly oriented samples, the saturation behavior of an MCD transition between spatially nondegenerate states A and J can be modeled in terms of the effective transition moment, M_{ij}^{eff} , between states A and J and the expectation values of the spin operators entering the spin-Hamiltonian describing the paramagnetic ground state. In the case of orthorhombic D_{2h} point group symmetry, the MCD magnetization curves can be fitted by the following expression:¹⁶

$$\frac{\Delta\epsilon}{E} = \frac{\gamma}{4\pi S} \int_0^\pi \int_0^{2\pi} \sum_i N_i (l_x \langle S_x \rangle_i M_{yz}^{\text{eff}} + l_y \langle S_y \rangle_i M_{zx}^{\text{eff}} + l_z \langle S_z \rangle_i M_{xy}^{\text{eff}}) \sin(\theta) d\theta d\varphi \quad (2)$$

where $\Delta\epsilon$ measures the difference in absorption between left and right circularly polarized light, E is the transition energy, γ is a collection of constants,¹⁶ S is the total spin of the ground state, N_i is the Boltzmann population of the i th Zeeman sublevel of the paramagnetic ground state, $l_{x,y,z}$ are the direction cosines with respect to the molecular frame of reference (x,y,z) with θ, φ being the angle of the projection of the light propagation direction with the z and y molecular axes, respectively, M_{jk}^{eff} is the effective transition moment defined elsewhere,¹⁶ and $\langle S_{x,y,z} \rangle$ is the expectation values of the spin operators $\hat{S}_x, \hat{S}_y, \hat{S}_z$, entering the spin-Hamiltonian eq 1 describing the paramagnetic ground state. These expectation values can be obtained by diagonalization of spin-Hamiltonian eq 1 in the subspace spanned by

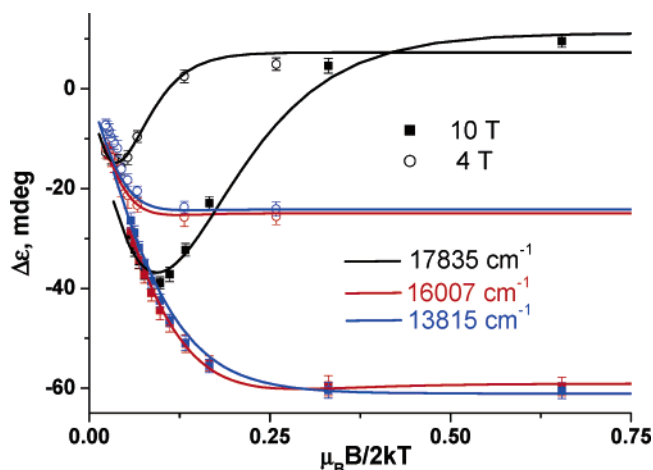


Figure 4. MCD saturation behavior of the selected transitions displayed by **2** in the visible region. The corrected experimental data (black, red, and blue for MCD transitions at 17835, 16007, and 13815 cm^{-1} , respectively) are shown as points (■ at 10 T and ○ at 4 T) accompanied by error bars corresponding to the 99.73% confidence interval (3σ). The simulated curves computed with the best fit parameters: $M_{xy}^{\text{eff}} = 0.650$, $M_{yz}^{\text{eff}} = 0.009$, and $M_{zx}^{\text{eff}} = -0.066$ (17 835 cm^{-1}); $M_{xy}^{\text{eff}} = -0.177$, $M_{yz}^{\text{eff}} = -0.219$, and $M_{zx}^{\text{eff}} = -0.007$ (16 007 cm^{-1}); $M_{xy}^{\text{eff}} = 0.001$, $M_{yz}^{\text{eff}} = -0.115$, and $M_{zx}^{\text{eff}} = 0.076$ (13 815 cm^{-1}); and $g = 2.14$, $D = +32 \text{ cm}^{-1}$, and $E/D = 0.1$ for all three bands are shown as solid lines.

the $2S + 1$ Zeeman sublevels of the paramagnetic ground state. Through the spin-expectation values as well as the Boltzmann populations, the spin-Hamiltonian parameters g , D , and E are introduced in the fitting model of the MCD magnetization curves (eq 2). In Figure 4, the saturation behavior of the three most prominent MCD bands centered at 13 815, 16 007, and 17 835 cm^{-1} (bands 2, 5, and 6, respectively, in Figure 8) in the MCD spectrum of **2** is shown. The intensity of each of these MCD bands was monitored for two different values of external applied magnetic field (4 and 10 T) and for temperatures ranging from 1.6 to 58 K. The experimental data (corrected for baseline effects and after subtraction of a spectrum extrapolated to infinite temperature) were fit according to eq 2. The best fit parameters for these three bands are: $M_{xy}^{\text{eff}} = 0.650$, $M_{yz}^{\text{eff}} = 0.009$, and $M_{zx}^{\text{eff}} = -0.066$ (band 6), $M_{xy}^{\text{eff}} = -0.177$, $M_{yz}^{\text{eff}} = -0.219$, and $M_{zx}^{\text{eff}} = -0.007$ (band 5), $M_{xy}^{\text{eff}} = 0.001$, $M_{yz}^{\text{eff}} = -0.115$, and $M_{zx}^{\text{eff}} = 0.076$ (band 2). Excellent fits to the data were obtained with $g = 2.14$, $D = +32 \text{ cm}^{-1}$ and $E/D = 0.1$ for all three bands. These results are in very good agreement with the spin-Hamiltonian parameters derived from magnetization and far-infrared measurements.

Mössbauer Spectroscopy. The zero-field Mössbauer spectrum of **1** displays a single quadrupole doublet with the parameters given in Table 2, which are in excellent agreement with those reported for $[\text{N}(\text{CH}_3)_4]_2[\text{Fe}(\text{L})_2]$.² Figure 5 shows the applied field spectra of **1** at 4.2 K and 1.0, 4.0, and 7.0 T. With D and E/D parameters from the magnetization data fixed at $+28 \text{ cm}^{-1}$ and 0.08, respectively, a good simulation of the experimental spectra was obtained with the following fit parameters: $\delta = 0.45 \text{ mm s}^{-1}$; $\Delta E_Q = 1.21 \text{ mm s}^{-1}$; $\eta = 0.44$; $A_{xx}/g_N\beta_N = -4.15 \text{ T}$, $A_{yy}/g_N\beta_N = -5.58 \text{ T}$, and $A_{zz}/g_N\beta_N = 0.18 \text{ T}$. By using a negative ZFS parameter, $D = -28 \text{ cm}^{-1}$, we did not obtain a satisfactory fit. It is noted that the alternative description of the ground state of **1** in terms of an $S = 0$ ground state thermally admixed to an energetically low-lying excited $S = 1$ state⁹ is

(33) Barraclough, C. G.; Martin, R. L.; Mitra, S. J. *Chem. Phys.* **1970**, *53*, 1643.
 (34) Krzystek, J.; Zvyagin, S. A.; Ozarowski, A.; Fiedler, A. T.; Brunold, T. C.; Telser, J. *J. Am. Chem. Soc.* **2004**, *126*, 2148.

Table 2. Calculated and Experimental Mössbauer Parameters for Salts Containing the Dianion $[\text{Fe}^{\text{II}}(\text{L})_2]^{2-}$

complex	T K	δ mm s^{-1}	ΔE_Q mm s^{-1}	η
$[\text{HN}(\text{Et})_3]_2[\text{Fe}(\text{L})_2]$	80	0.44	1.19	
	4.2	0.44	1.22	0.44
$[\text{N}(n\text{-Bu})_4]_2[\text{Fe}(\text{L})_2]$	80	0.46	1.08	
	4.2	0.47	1.09	n.d. ^b
$[\text{N}(\text{CH}_3)_4]_2[\text{Fe}(\text{L})_2]^a$	293	0.37	1.12	
	85	0.435	1.16	
	4.2	0.44	1.16	n.d. ^b
$[\text{Fe}(\text{L})_2]^{2-}$ (calcd, nonrelativistic B3LYP DFT methods)		0.41	0.68	0.48
$[\text{Fe}(\text{L})_2]^{2-}$ (calcd, scalar relativistic ZORA B3LYP DFT methods)		0.38	0.94	0.46

^a Reference 2. ^b n.d. = not determined.

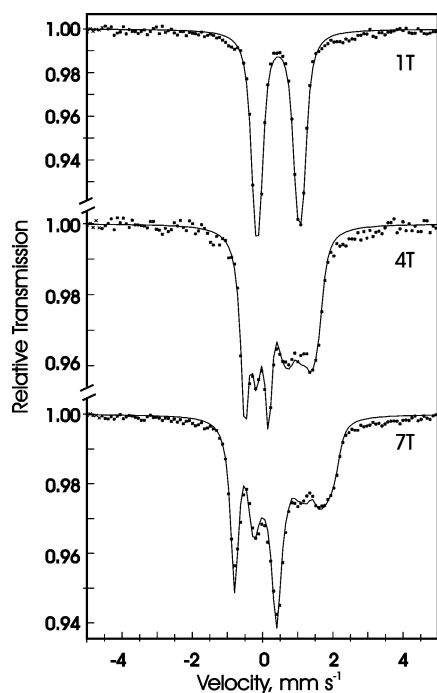


Figure 5. Applied magnetic field Mössbauer spectra of **1** at 4.2 K. Fit parameters: $\delta = 0.45 \text{ mm s}^{-1}$; $\Delta E_Q = 1.21 \text{ mm s}^{-1}$; $A_{xx}/g_N\beta_N = -4.15 \text{ T}$, $A_{yy}/g_N\beta_N = -5.58 \text{ T}$, $A_{zz}/g_N\beta_N = 0.18 \text{ T}$; $D = +28 \text{ cm}^{-1}$ (fixed); $E/D = 0.08$ (fixed).

not in accord with the observed temperature independence of the quadrupole splitting.

Crystal Structures

Table 3 summarizes selected bond lengths and angles of the anions in **1** and **2a**; Figure 6 shows the anion in **1** and that in **2a**. Crystals of **1** consist of the cation $[\text{HN}(\text{C}_2\text{H}_5)_3]^+$ and the dianion $[\text{Fe}^{\text{II}}(\text{L})_2]^{2-}$ (ratio 2:1). The dianion is as in $[\text{AsPh}_4]_2[\text{Fe}^{\text{II}}(\text{L})_2]$ planar.¹ Interestingly, the two monocations are $\text{N}\cdots\text{H}\cdots\text{S}$ hydrogen bonded to two coordinated sulfur atoms of a single dianion as shown in Figure 6. The $\text{N}\cdots\text{S}$ distances are at $3.252(3) \text{ \AA}$. In the solid state these ion pairs, $\{[\text{HN}(\text{C}_2\text{H}_5)_3]_2[\text{Fe}^{\text{II}}(\text{L})_2]\}^0$, are packed via intermolecular van der Waals contacts. The shortest intermolecular $\text{Fe}\cdots\text{Fe}$ and $\text{Fe}\cdots\text{S}$ distances are at 7.380 and 7.185 \AA , respectively. Clearly, there is no detectable pathway for a significant intermolecular spin exchange, be it antiferro- or ferromagnetic. Thus, the observed temperature-dependent decrease of μ_{eff} at temperatures $< 50 \text{ K}$ (Figure 2) cannot be explained by intermolecular magnetic

Table 3. Selected Bond Lengths (\AA) and Angles (deg) of the Anions in Crystals of **1** and **2a**

Complex 1			
Fe–S1	2.2263(3)	S2–Fe–S2*	180.0
Fe–S2	2.2242(3)	S2–Fe–S1	89.97(1)
S1–C1	1.772(1)	S2–Fe–S1*	90.03(1)
C1–C6	1.402(2)		
C1–C2	1.406(2)		
S2–C2	1.765(1)		
C2–C3	1.403(2)		
C3–C4	1.392(2)		
C4–C5	1.395(2)		
C5–C6	1.392(2)		
Complex 2a			
Co(1)–S(2)	2.1396(8)	Co(1)–S(4)	2.1496(8)
Co(1)–S(1)	2.1662(8)	Co(1)–S(3)	2.1653(8)
S(1)–C(1)	1.772(3)	S(2)–C(6)	1.753(3)
S(3)–C(21)	1.770(3)	S(4)–C(26)	1.757(3)
C(1)–C(6)	1.394(4)	C(1)–C(2)	1.418(4)
C(5)–C(6)	1.393(4)	C(4)–C(5)	1.376(4)
C(3)–C(4)	1.396(4)	C(2)–C(3)	1.397(4)
C(21)–C(26)	1.405(4)	C(21)–C(22)	1.420(4)
C(25)–C(26)	1.386(4)	C(24)–C(25)	1.381(4)
C(23)–C(24)	1.404(4)	C(22)–C(23)	1.394(4)
S2–Co–S4	89.35(3)	S2–Co–S3	174.86(4)
S4–Co–S3	90.95(3)	S2–Co–S1	90.40(3)
S4–Co–S1	176.23(3)	S3–Co–S1	89.64(3)

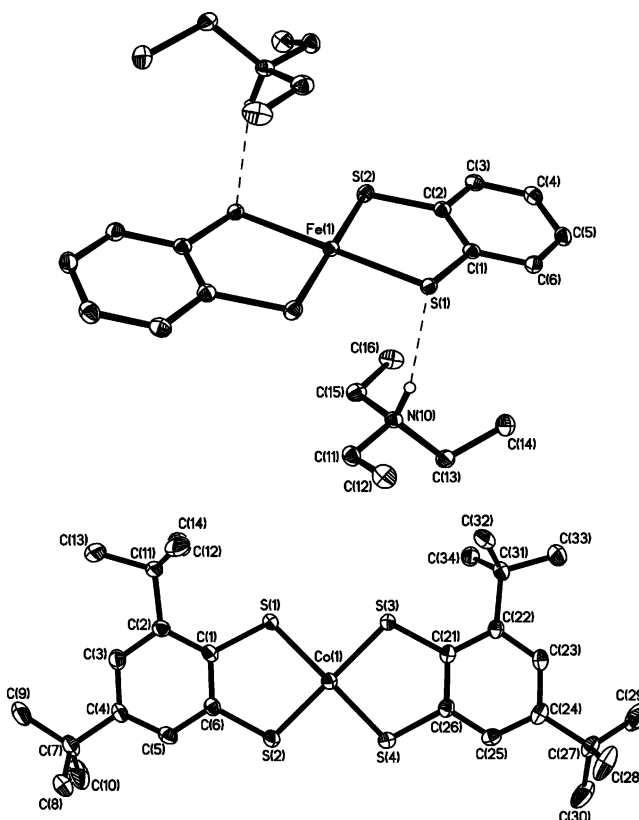


Figure 6. Structures of the ion pair $[\text{NH}(\text{Et})_3][\text{Fe}^{\text{II}}(\text{L})_2]$ in crystals of **1** (top) and of the monoanion $[\text{Co}^{\text{III}}(\text{L}^{\text{Bu}})_2]^-$ in crystals of **2a**.

ordering effects in the solid state. It is remarkable that both crystallographically independent Fe–S distances in **1** are identical within experimental error at $\text{av } 2.225 \pm 0.001 \text{ \AA}$. In Sellmann's complex $[\text{AsPh}_4]_2[\text{Fe}(\text{S}_2\text{C}_6\text{H}_4)_2]$ the average Fe–S distance is the same at $2.226 \pm 0.001 \text{ \AA}$. This clearly indicates that the presence of weak $\text{N}\cdots\text{H}\cdots\text{S}$ hydrogen bonding in **1** does not influence the Fe–S bond length.

The C–C bond lengths in the benzene-1,2-dithiolato anions are within experimental error of $\pm 0.006 \text{ \AA}$ (3σ) identical at an average of 1.398 \AA , which clearly indicates the aromatic

character of these phenyl rings. The two C–S bonds of an S,S' -coordinated ligand are not identical at 1.772(1) and 1.765(1) Å because the sulfur atom of the longer C–S bond is involved in the N–H···S hydrogen bonding scheme, whereas the other, shorter one is not. C–S bonds at $\sim 1.76 \pm 0.01$ Å are indicative of single bonds. Therefore, we can safely conclude that the benzene-1,2-dithiolate ligands in **1** are closed-shell aromatic dianions. This renders the iron ion a +II spectroscopic oxidation state with a d^6 electron configuration. According to simple ligand field considerations, such a d^6 configuration in a square-planar ligand field should possess an $S = 1$ ground state as is observed. Note that the corresponding, square-planar monoanion $[\text{Au}^{\text{III}}(\text{L})_2]^-$ with a d^8 configuration is diamagnetic ($S = 0$).³⁵ Here also the six C–C distances are equidistant (av 1.395 \pm 0.01 Å) and the two C–S bonds are identical at 1.762 \pm 0.006 Å.

Crystals of **2** consist of the monocation $[\text{N}(n\text{-Bu})_4]^+$ and the square-planar monoanion $[\text{Co}^{\text{III}}(\text{L}^{\text{Bu}})_2]^-$ (ratio 1:1). It is noteworthy that the two S,S' -coordinated ligands adopt a cis conformation relative to each other. The anion is not perfectly square-planar. The dihedral angle between the two aromatic phenyl rings is 6.3°. The individual monoanions are well-separated in the solid state; intermolecular interactions leading to spin coupling phenomena cannot be identified.

The six C–C bond lengths of the phenyl rings are not quite equidistant, which is because a tertiary butyl group is in ortho position relative to one thiolate sulfur atom but the second *tert*-butyl group is in meta position relative to the second sulfur atom. Thus, steric repulsion may be anticipated for the first case but not for the second. Thus, the bonds C1–C2 and C21–C22 are the longest at 1.42 \pm 0.01 Å; the average of the other five C–C distances is 1.393 \pm 0.01 Å. The average C–S bond is again long at 1.76 \pm 0.01 Å. These data appear to indicate that both ligands are S,S' -coordinated, closed-shell dianions $(\text{L}^{\text{Bu}})^{2-}$, and consequently, the central cobalt ion possesses a formal oxidation state of +III with a d^6 electron configuration in a square-planar ligand field yielding an $S = 1$ ground state.

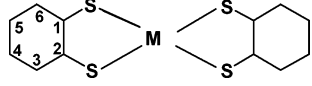
Interestingly, in a recent publication, Almeida et al.³⁶ describe the crystal structure of deep-blue $[\text{N}(n\text{-Bu})_4]_2[\text{Co}^{\text{II}}(\text{L}'')_2]$ ($S = 1/2$) containing the dianion $[\text{Co}^{\text{II}}(\text{L}'')_2]^{2-}$, where $(\text{L}'')^{2-}$ is the 4,5-dicyanobenzene-1,2-dithiolate(2-) ligand. The average Co–S distance is at 2.179(1) Å, which is longer than that in **2** at 2.153-(1) Å by 0.026 Å. This reflects a small metal-centered reduction effect on going from low-spin Co^{II} to intermediate-spin Co^{III} .

DFT Calculations

In this section, a detailed picture of the electronic structure of the monoanionic complex $[\text{Co}(\text{L})_2]^{1-}$ and of the dianionic species $[\text{Fe}(\text{L})_2]^{2-}$ is derived from DFT calculations. These calculations lead to a bonding scheme that provides a better understanding of this fascinating class of isoelectronic, square-planar complexes. Particular efforts are directed toward an understanding of (a) the origin of the large ZFS and (b) the origin of the differences between the absorption spectra of these two isoelectronic complexes.

(a) Calculated Geometries. The calculated geometries are found to be in good agreement with the experimental data (Table

Table 4. Experimental (in Parentheses) and Calculated Bond Lengths (Å) in $[\text{Co}(\text{L})_2]^{1-}$ and $[\text{Fe}(\text{L})_2]^{2-}$ Obtained by DFT Calculations at the Scalar Relativistic DKH2-BP86 Level



	$[\text{Fe}(\text{L})_2]^{2-}$	$[\text{Co}(\text{L})_2]^{1-}$
M–S	2.229(2.225(1)) ^a	2.184(2.155(1)) ^b
C–S	1.788(1.768(2))	1.781(1.763(3))
C ₁ –C ₂	1.401(1.406(2))	1.408(1.418(4))
C ₂ –C ₃	1.394(1.403(2))	1.395(1.397(4))
C ₃ –C ₄	1.392(1.392(3))	1.396(1.396(4))
C ₄ –C ₅	1.398(1.395(3))	1.390(1.376(4))

^a Experimental bond length for **1**. ^b Experimental bond length for **2a**.

4) for both species. The M–S bond lengths are slightly overestimated (by +0.03 Å) in the cobalt case, but they are accurately predicted for the iron complex. The most revealing bonds are the C–S and the ring C–C distances, which are both accurately predicted in the calculations with the typical error <0.01 Å for both species. In each case, long C–S bonds (~ 1.77 Å) and essentially equivalent C–C distances (1.40 Å) within the aromatic rings are observed. These results suggest the absence of 1,2-dithiobenzosemiquinonato(1-) radical anion character in these complexes.

(b) Bonding Scheme. The bonding scheme of the corresponding square-planar complex $[\text{Co}(\text{L}_N)_2]^{1-}$ has been described recently,³⁷ where $(\text{L}_N)^{2-}$ represents the N,N' -coordinated *N*-phenyl-*o*-phenylenediamide(2-) ligand. The electronic structure of the complex was difficult to understand, even qualitatively, because the out-of-plane orbital $2b_{2g}$ had almost equal contributions from the Co $3d_{xz}$ and the b_{2g} ligand fragment orbitals. It was therefore not possible to assign straightforwardly a spectroscopic oxidation state for the cobalt ion (d^6 or d^7). Thus, the actual electronic structure of the complex was best represented by the following resonance forms $[\text{Co}^{\text{III}}(\text{L}^{2-})(\text{L}^{2-})]^- \leftrightarrow [\text{Co}^{\text{II}}(\text{L}^{\bullet-})(\text{L}^{2-})]^- \leftrightarrow [\text{Co}^{\text{II}}(\text{L}^{2-})(\text{L}^{\bullet-})]^-$ with a somewhat larger weight for the first resonance structure.

The situation is similar for the $[\text{Co}(\text{L})_2]^{1-}$ complex. The calculated ground state is $^3\text{B}_{1g}$ with the following electronic configuration:

$$(1a_g)^2 (2a_g)^2 (1b_{3g})^2 (1a_u)^2 (1b_{2g})^2 (1b_{1u})^2 (2b_{2g})^1 (2b_{3g})^1 (1b_{1g})^0$$

The qualitative bonding scheme for the $[\text{Co}(\text{L})_2]^{1-}$ complex derived here from the spin-unrestricted B3LYP DFT calculations is found to be identical to that of $[\text{Co}(\text{L}_N)_2]^{1-}$; it is shown in Figure 7. The ligand character in the $2b_{2g}$ orbital is again found to be quite high (36%) (Table 5), and therefore, the description of the electronic structure of this monoanionic species as containing an intermediate-spin $\text{Co}(\text{III})$ ion coordinated to two dianionic benzene-1,2-dithiolate ligands, $(\text{L})^{2-}$, is somewhat ambiguous.

It is interesting to compare the electronic structure of $[\text{Co}(\text{L})_2]^{1-}$ with that of the isoelectronic $[\text{Fe}(\text{L})_2]^{2-}$. The qualitative bonding scheme derived from the spin-unrestricted B3LYP DFT calculations of the iron compound is also shown in Figure 7. The calculated ground state is also found to be

(35) Ray, K.; Weyhermüller, T.; Goossens, A.; Craje, M. W. J.; Wieghardt, K. *Inorg. Chem.* **2003**, *42*, 4083.

(36) Alves, H.; Simao, D.; Santos, I. C.; Gama, V.; Henriques, R. T.; Novais, H.; Almeida, M. *Eur. J. Inorg. Chem.* **2004**, 1318.

(37) Bill, E.; Bothe, E.; Chaudhuri, P.; Chlopek, K.; Herebian, D.; Kokatam, S.; Ray, K.; Weyhermüller, T.; Neese, F.; Wieghardt, K. *Chem.–Eur. J.* **2004**, *11*, 204.

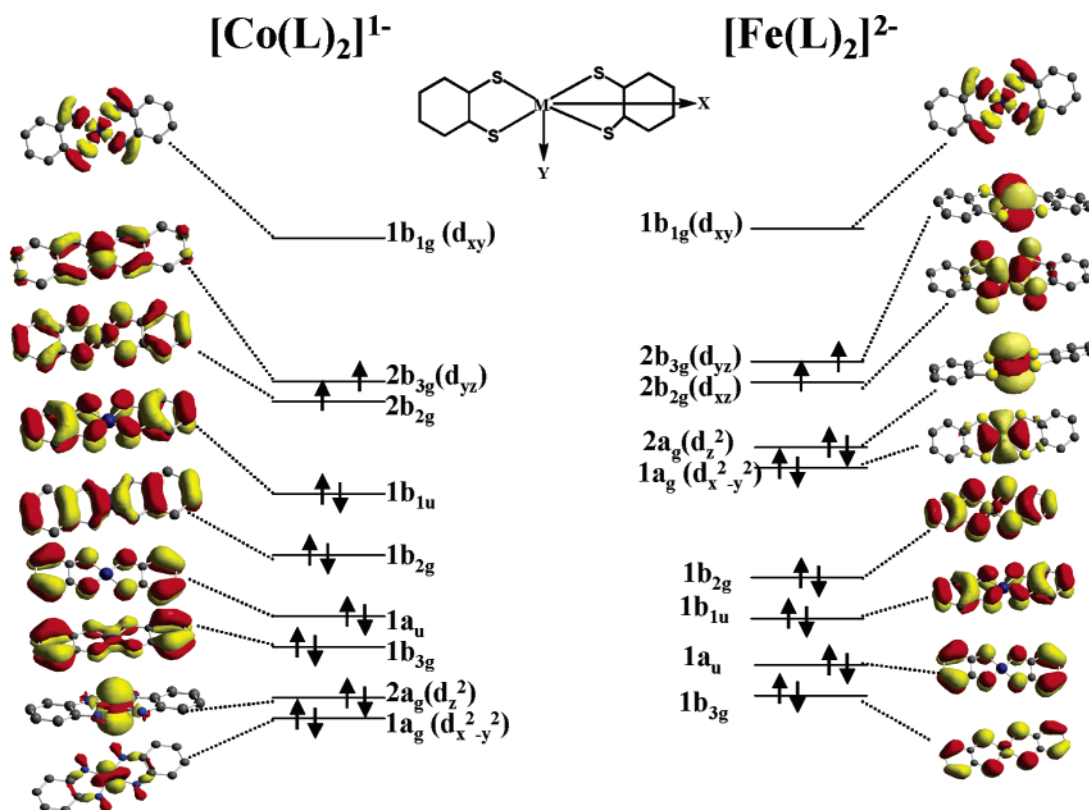


Figure 7. Kohn–Sham MO orbitals and energy scheme of $[\text{Co}(\text{L})_2]^{1-}$ and $[\text{Fe}(\text{L})_2]^{2-}$ from spin-unrestricted scalar relativistic ZORA-B3LYP DFT methods.

Table 5. Percentage Composition of the Selected Orbitals of $[\text{Co}(\text{L})_2]^{1-}$ and $[\text{Fe}(\text{L})_2]^{2-}$ as Obtained from DFT (COSMO) Calculation at the Scalar Relativistic ZORA-B3LYP Level Using CH_2Cl_2 as the Solvent

complex	MO	M(3d _{yz})	M(3d _{xz})	S(2p _z)	C(2p _z)
$[\text{Co}(\text{L})_2]^{1-}$	2b _{3g}	76		10	10
	2b _{2g}		65	28	08
$[\text{Fe}(\text{L})_2]^{2-}$	2b _{3g}	90		3	2
	2b _{2g}		82	8	6

Table 6. Comparison of the Charge and Spin Populations at the Metal Ion Resulting from a Natural Population Analysis of the One-Electron Density of the Ground State Resulting from Scalar Relativistic ZORA-B3LYP DFT Calculations in CH_2Cl_2 Solution by Using COSMO Model

	electrons-d	electrons-4s	spin-d	spin-s
$[\text{Co}(\text{L})_2]^{1-}$	7.82	0.51	1.59	0.00
$[\text{Fe}(\text{L})_2]^{2-}$	7.11	0.49	1.92	0.00

$^3\text{B}_{1g}$ with the ground-state electronic configuration of

$$(1b_{3g})^2 (1a_u)^2 (1b_{1u})^2 (1b_{2g})^2 (1a_g)^2 (2a_g)^2 (2b_{2g})^1 (2b_{3g})^1 (1b_{1g})^0$$

Despite this formally identical ground-state electronic configuration, there is an important difference in the bonding schemes. In $[\text{Fe}(\text{L})_2]^{2-}$ the Fe 3d_{x²-y²} (1a_g) and 3d_{z²} (2a_g) orbitals are shifted to higher energy as compared to the corresponding orbitals for $[\text{Co}(\text{L})_2]^{1-}$. As shown in Table 5, the 2b_{3g} SOMO is predominantly metal-centered in both the $[\text{Fe}(\text{L})_2]^{2-}$ and the $[\text{Co}(\text{L})_2]^{1-}$, whereas the 2b_{2g} SOMO is essentially metal-centered (82% metal 3d_{xz}) in $[\text{Fe}(\text{L})_2]^{2-}$ but possesses significant contributions from both metal and ligand in the cobalt case (only 65% metal 3d_{xz}). The predominance of the metal character in the 2b_{2g} level of $[\text{Fe}(\text{L})_2]^{2-}$ arises from the lower effective nuclear charge (Z_{eff}) of Fe as compared to Co, which brings the Fe 3d levels higher in energy and makes them less available for back-bonding interactions with the ligand orbitals. The upper valence region of the iron complex is therefore composed of two doubly occupied and two singly occupied orbitals that are predominantly centered on iron. Thus, the electronic structure of the complex can be understood in terms of an intermediate-spin (d⁶, $S = 1$) ferrous ion ligated by two innocent benzene-1,2-dithiolate(2-) ligands.

It is also useful to compare the calculated ground-state electron and spin distribution from the B3LYP natural population analysis³⁰ between the $[\text{Co}(\text{L})_2]^{1-}$ and the $[\text{Fe}(\text{L})_2]^{2-}$ species (Table 6). For the $[\text{Fe}(\text{L})_2]^{2-}$ species, the analysis shows a d-population of 7.11 and a spin density of 1.92 at the central iron ion. Both values are consistent with an intermediate-spin Fe(II) center and matches the spectroscopic data obtained for this complex. The charge excess over the formal d⁶ electron configuration arises from the covalent population of the otherwise unpopulated Fe d_{xy} orbital due to strong σ -donation from the ligand. However, for the $[\text{Co}(\text{L})_2]^{1-}$ complex the calculated d-population of 7.82 and the spin density of 1.59 show it to be more reduced than typical Co(III) and more oxidized than typical Co(II) complexes. Thus, in $[\text{Co}(\text{L})_2]^{1-}$ the cobalt seems to have a character between Co(II) (d⁷) and Co(III) d⁶. This can be best represented by the resonance forms $[\text{Co}^{\text{III}}(\text{L}^{2-})(\text{L}^{2-})]^{-} \leftrightarrow [\text{Co}^{\text{II}}(\text{L}^{\bullet-})(\text{L}^{2-})]^{-} \leftrightarrow [\text{Co}^{\text{II}}(\text{L}^{2-})(\text{L}^{\bullet-})]^{-}$. Thus, the situation is found to be similar to that of the $[\text{Co}(\text{L}_N)_2]^{1-}$ complex.³⁷ However, in the calculation the Co(III) character is more pronounced in $[\text{Co}(\text{L})_2]^{1-}$ than in $[\text{Co}(\text{L}_N)_2]^{1-}$ as is evident from the enhanced metal character of the 2b_{2g} SOMO and larger spin density at the Co ion in $[\text{Co}(\text{L})_2]^{1-}$.

(c) Ground-State Spectroscopic Parameters. Mössbauer Parameters. The Mössbauer isomer shift, δ , the quadruple

splitting parameter, ΔE_{O} , and the asymmetry parameter, η , have been calculated for the $[\text{Fe}(\text{L})_2]^{2-}$ species by using both scalar relativistic ZORA and nonrelativistic B3LYP DFT methods as discussed in ref 38. The isomer shift is reasonably well-predicted in both sets of calculations (Table 2). On the other hand, the quadrupole splitting is overestimated in the nonrelativistic calculation but it is accurately predicted on applying the relativistic correction for the central iron atom. We conclude from this result and the good agreement between calculated and experimental structure parameters that the calculations faithfully describe the electronic structure of the $[\text{Fe}(\text{L})_2]^{2-}$ species.

Zero-Field Splitting. We also attempt to understand the origin of the large positive ZFS for the $[\text{Fe}(\text{L})_2]^{2-}$ and the $[\text{Co}(\text{L})_2]^{1-}$ species on the basis of the DFT calculations. The terms that are candidates for contributing to the ZFS are the first-order terms arising from the spin–spin dipolar interactions and the second-order contributions arising from SOC of the ground and the excited states. It is well-known that the direct spin–spin dipolar interaction gives a traceless first-order contribution,³⁹ and for transition-metal complexes it is generally assumed that the second-order contribution to the **D**-tensor is dominant.⁴⁰

The original derivation of the second-order contribution to the **D**-tensor has been described in detail elsewhere.²⁶ The derivation shows that, to second-order contributions, the **D**-tensor has three contributions that come from excited states either with the same spin as the ground state or with the total spin quantum number increased or decreased by one relative to the ground state. Such excited states may be derived from either of the following transitions: (i) by promoting a single spin down (*beta*) electron from a doubly occupied molecular orbital (DOMO) into one of the singly occupied molecular orbitals (SOMOs), giving rise to states of the same spin multiplicity as the ground state. The transition is therefore termed as a *beta–beta* transition. (ii) An *alpha–alpha* transition can be derived by promotion of an electron from a SOMO to a virtual molecular orbital (VMO), again resulting in states of the same spin multiplicity as the ground state. (iii) A spin flip transition (*beta–alpha*) from a DOMO to a VMO gives rise to states of higher spin multiplicity than the ground state. (iv) Finally, promoting an electron from one of the SOMOs into another SOMO with an accompanying spin flip (*alpha–beta*) gives rise to states of lower spin multiplicity than the ground state. These excited states can be crudely mimicked in DFT through a sum over orbital pairs arising from a suitable open-shell spin-restricted treatment. The resulting method is not strictly a DFT response theory but is expected to mimic it closely as can be verified from comparison of the calculated *g*-tensors at the same level of approximation which agree closely with those obtained from coupled-perturbed SCF theory.⁴¹

The **D**-tensors for the $[\text{Fe}(\text{L})_2]^{2-}$ and the $[\text{Co}(\text{L})_2]^{1-}$ species have been calculated by DFT methods that include all the above-mentioned SOC contributions to the ZFS but neglect the direct

Table 7. The Calculated Axial (*D*) and Rhombic (*E*) Zero-Field Splitting Parameters for the Complexes Obtained from the Quasi-Restricted DFT Calculations at the Scalar Relativistic ZORA-BP86 Level in CH_2Cl_2 Solution Using the COSMO Model and Their Comparison to Experiments

compd	<i>D</i> cm ⁻¹		<i>E/D</i>		<i>g</i> _{so}	
	expt	calcd	expt	calcd	expt	calcd
$[\text{Fe}(\text{L})_2]^{2-}$	+28	+18	0.08	0.05	2.05	2.07
$[\text{Co}(\text{L})_2]^{1-}$	+32	+26	0.11	0.11	2.16	2.10

Table 8. Contributions of the Different Excitation Classes (in cm⁻¹) to the Axial (*D*) and Rhombic (*E*) Zero-Field Splitting for the $[\text{Co}(\text{L})_2]^{1-}$ and the $[\text{Fe}(\text{L})_2]^{2-}$ Species as Obtained from the Quasi-Restricted DFT Calculations at the Scalar Relativistic ZORA-BP86 Level in CH_2Cl_2 Solution Using the COSMO Model

complex	excitation class	<i>D</i> (cm ⁻¹)	<i>E</i> (cm ⁻¹)
$[\text{Co}(\text{L})_2]^{1-}$	SOMO → VMO (alpha → alpha)	2.699	-0.113
	DOMO → SOMO (beta → beta)	14.891	2.964
	SOMO → SOMO (alpha → beta)	5.907	-0.000
	DOMO → VMO (beta → alpha)	1.823	-0.143
$[\text{Fe}(\text{L})_2]^{2-}$	SOMO → VMO (alpha → alpha)	2.417	-0.081
	DOMO → SOMO (beta → beta)	10.865	0.836
	SOMO → SOMO (alpha → beta)	3.226	-0.000
	DOMO → VMO (beta → alpha)	1.823	-0.127

spin–spin coupling. It is gratifying that both the sign and the magnitude of the calculated **D**-tensors are in reasonable agreement with the experiments (Table 7). The analysis of the contributions of the different excitation classes (Table 8) to the **D**-tensor shows that the main contribution comes from the excitations of the type DOMO to SOMO for both species, that is, spin-conserving excitations. The dominant contribution involves the promotion of an electron from the doubly occupied $2a_g$ (d_z^2) and $1a_g$ ($d_{x^2-y^2}$) orbitals to the singly occupied $2b_{3g}$ (d_{yz}) and $2b_{2g}$ (d_{xz}) orbitals giving rise to excited states that can spin–orbit couple with the $^3B_{1g}$ ground states via the l_x or l_y component of the spin–orbit coupling operator (Table 8). These transitions correspond to low-energy excitations, but they account predominantly for the large magnitude of the ZFS in both $[\text{Fe}(\text{L})_2]^{2-}$ and $[\text{Co}(\text{L})_2]^{1-}$. The transitions that are next of significance involve the spin flip excitations between the two SOMOs, $2b_{2g}$ and $2b_{3g}$, giving rise to low-lying states of symmetry $^1B_{2g}$ and $^1B_{3g}$, which can again spin–orbit couple to the $^3B_{1g}$ ground state. All the other transitions have minor contributions to the **D**-tensors (Table 8).

Thus, in $[\text{Fe}(\text{L})_2]^{2-}$ and $[\text{Co}(\text{L})_2]^{1-}$, the large ZFS mainly originates from the spin–orbit coupling of the ground state with the low-lying d–d excited states which are found at similar energies in both cases (Table 9). Hence, despite the fact that the Fe 3d orbitals are placed at a higher energy in $[\text{Fe}(\text{L})_2]^{2-}$ than the Co 3d orbitals in $[\text{Co}(\text{L})_2]^{1-}$, the destabilization takes place to a similar extent for all Fe 3d orbitals and, correspondingly, the nature of the d–d excitations are comparable in both species. This is also reflected in the similar magnitude of the *D* value in both cases. The larger value for the cobalt species can, however, be explained on the basis of the larger value of the one-electron SOC constant on Co (~ 600 cm⁻¹) as compared to that on Fe (~ 400 cm⁻¹).⁴² The variation of covalency, especially in the $2b_{2g}$ SOMO, on moving from the cobalt to the iron species has minor contribution in determining the variation of the magnitude of the ZFS in the two cases as can be verified

(38) (a) Neese, F. *Inorg. Chim. Acta*, **2002**, *337*, 181. (b) Sinnecker, S.; Slep, L.; Bill, E.; Neese, F. *Inorg. Chem.*, published online Feb. 26, 2005 <http://dx.doi.org/10.1021/ic048609e>.

(39) For a recent review, see: Neese, F. In *Calculation of NMR and EPR Parameters*; Kaupp, M.; Malkin V., Bühl, M., Eds.; Wiley-VCH: Weinheim, Germany, 2004; pp 541.

(40) Griffith, J. S. *The Theory of Transition Metal Ions*; Cambridge University Press: Cambridge, 1964.

(41) Neese, F. *J. Chem. Phys.* **2001**, *115*, 11080.

(42) Bendix, J.; Brorson, M.; Schäffer, C. E. *Inorg. Chem.* **1993**, *32*, 2838.

Table 9. Spin–Orbit Coupling (SOC) Matrix Elements and the Corresponding Energies for the Excitations Contributing to the Large Zero-Field Splittings in $[\text{Co}(\text{L})_2]^{1-}$ and $[\text{Fe}(\text{L})_2]^{2-}$ as Obtained from the Quasi-Restricted DFT Calculations at the Scalar Relativistic ZORA-BP86 Level^a

excitation class	excitations	$[\text{Co}(\text{L})_2]^{1-}$		$[\text{Fe}(\text{L})_2]^{2-}$	
		SOC (cm^{-1})	ΔE (cm^{-1})	SOC (cm^{-1})	ΔE (cm^{-1})
DOMO \rightarrow SOMO	$1a_g(d_{x^2-y^2}) \rightarrow 2b_{3g}(d_{yz})$	689	13293	475	13518
	$2a_g(d_{z^2}) \rightarrow 2b_{3g}(d_{yz})$	536	8412	518	9774
	$1a_g(d_{x^2-y^2}) \rightarrow 2b_{2g}(d_{xz})$	132	16074	207	15735
	$2a_g(d_{z^2}) \rightarrow 2b_{2g}(d_{xz})$	711	11186	314	11791
SOMO \rightarrow SOMO	$2b_{3g}(d_{yz}) \rightarrow 2b_{2g}(d_{xz})$	356	18267	358	22848
	$2b_{2g}(d_{xz}) \rightarrow 2b_{3g}(d_{yz})$	356	4387	358	9597

^a Calculations are performed using the COSMO model in CH_2Cl_2 solution.

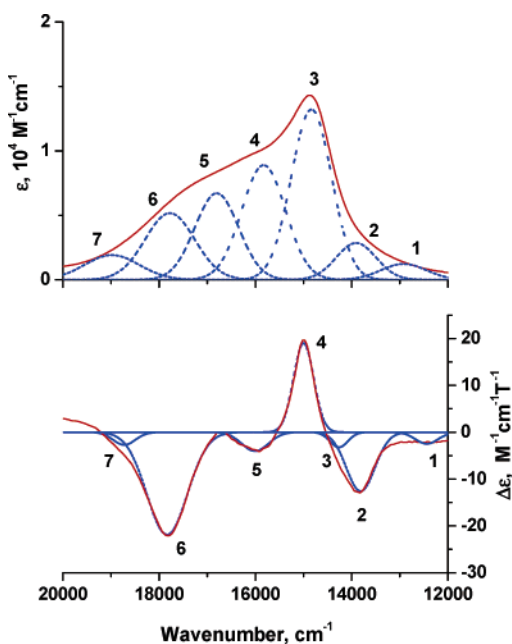


Figure 8. Deconvoluted room-temperature electronic absorption spectrum of **2** (top) and its MCD spectrum (bottom) recorded at 32 K and 5 T.

from inspection of individual spin–orbit coupling matrix elements that enter the calculation (Table 9).

(d) Excited-State Calculations and Assignments. On the basis of the success of the ground-state calculations, TD-DFT calculations have been performed to interpret the striking differences in the absorption spectra of the $[\text{Fe}(\text{L})_2]^{2-}$ and the $[\text{Co}(\text{L})_2]^{1-}$ species.

The room-temperature absorption and low-temperature MCD spectra of $[\text{Co}(\text{L})_2]^{1-}$ have been subjected to Gaussian deconvolution in the range 22 000–10 000 cm^{-1} to detect the individual transitions (Figure 8). As is commonly observed, the bands show a slight shift on going from ambient to liquid helium temperature, and therefore, equal band positions have not been enforced in the fit. The minimum number of Gaussian bands was used that is consistent with the experimentally observed peaks and shoulders, yielding a total of seven detectable transitions for $[\text{Co}(\text{L})_2]^{1-}$ below 22 000 cm^{-1} . The corresponding complex $[\text{Fe}(\text{L})_2]^{2-}$ does not show transitions in this range. Because of its extreme air sensitivity, it has not been possible to record the MCD spectrum of the $[\text{Fe}(\text{L})_2]^{2-}$ species.

In the D_{2h} point group, all transitions are unipolarized, and thus, spin–orbit coupling to other states with noncollinear transition moments is required to obtain nonzero MCD intensity.¹⁶ Since the SOC only couples states of like parity, it is either the SOC of the ground state with other “gerade” states

or the coupling of the electric dipole allowed excited states with other “ungerade” states that gives rise to the observed signs. As explained earlier for the $[\text{Co}(\text{L})_2]^{1-}$ species, there are low-lying d–d excited states present that can spin–orbit couple to the ground state giving rise to a large ZFS. Thus, one expects the ground-state SOC to also dominate the MCD response. This is consistent with the observed dominance of only one sign (negative) in the experimental MCD spectrum (Figure 8). The temperature dependence of the MCD spectrum (not shown) indicates that all observed features arise from a C-term mechanism that is expected to dominate for paramagnetic molecules studied at low temperature.

Time-dependent DFT calculations (using the B3LYP functional; quasi-relativistic ZORA method; large uncontracted Gaussian bases as described in the Experimental Section) for the $[\text{Co}(\text{L})_2]^{1-}$ species in CH_2Cl_2 solution have been performed by using the COSMO²⁹ model to account for the effects of solvation. Four LMCT states with reasonable intensities are calculated in the range 20 000–12 000 cm^{-1} , which nicely agrees with the four bands (bands 3, 4, 5, and 7) resolved in the simultaneous fit of the MCD and absorption spectra. In the experimental spectrum, LMCT bands are distinguished from their d–d counterparts on the basis of their lower C/D ratios (Table 10). In the calculation the most intense band arises from the $1b_{1u} \rightarrow 2b_{2g}$ transition, which corresponds to a LMCT transition of ${}^3B_{2u}$ symmetry and is allowed in the x-polarization. This transition is calculated at 19 050 cm^{-1} and is observed in the region of band 3 at 14 890 cm^{-1} , which is considered to be in reasonable agreement. The second transition calculated in the region of band 4 is the spin and electric dipole allowed $1a_u \rightarrow 2b_{2g}$ (${}^3B_{3u}$ symmetry, y-polarized) transition at 19 342 cm^{-1} with a calculated oscillator strength of 0.014. This is also in good agreement with the experimentally observed transition energy of 15 900 cm^{-1} and an oscillator strength of 0.044. The next transition is calculated at 19 560 cm^{-1} with an oscillator strength of 0.001. Its calculated symmetry is ${}^3B_{3u}$ ($1b_{1u} \rightarrow 2b_{3g}$) and is assigned to the reasonably intense band 5 observed at 16 804 cm^{-1} . Band 5 can obtain considerable intensity by mixing with the comparatively intense band 4, which has the same symmetry. The final transition below 22 000 cm^{-1} is calculated in the region of band 7 at 20 200 cm^{-1} (experimental transition energy 18 983 cm^{-1}) with an oscillator strength of 0.001 and corresponds to the electric dipole allowed $1a_u \rightarrow 2b_{3g}$ (${}^3B_{2u}$ symmetry, x-polarized) transition. Since its symmetry is ${}^3B_{2u}$ it can also gain considerable intensity by mixing with the intense LMCT $1b_{1u} \rightarrow 2b_{2g}$ band, which has the same symmetry.

Bands 1, 2, and 6 correspond to electric dipole forbidden d–d transitions as evident from their large C/D ratios (Table 10). In

Table 10. Analysis of the Optical Transitions for $[\text{Co}(\text{L})_2]^{1-}$ Following Gaussian Deconvolution of the ABS and MCD Spectra Shown in Figure 8 Combined with the Results of the Time-Dependent Density Functional COSMO Calculations in CH_2Cl_2 Solution at the Scalar Relativistic ZORA-B3LYP Level

band	energy [cm^{-1}]		method	oscillator strength		C/D	assignment
	expt	calcd		expt	calcd		
1	12921	8700	abs	0.006	0.00	-0.23	${}^3\text{B}_{2g}(2a_g(d_{xz}) \rightarrow 2b_{3g}(d_{yz}))$
	12439		MCD				
2	13908	11500	abs	0.013	0.00	-0.16	${}^3\text{B}_{3g}(2a_g(d_{xz}) \rightarrow 2b_{2g}(d_{xz}))$
	13815		MCD				
3	14890	19050	abs	0.060	0.132	-0.003	${}^3\text{B}_{2u}(1b_{1u} \rightarrow 2b_{2g}(d_{xz}))$
	14300		MCD				
4	15900	19342	abs	0.044	0.014	0.05	${}^3\text{B}_{3u}(1a_u \rightarrow 2b_{2g}(d_{xz}))$
	15000		MCD				
5	16804	19560	abs	0.033	0.001	-0.02	${}^3\text{B}_{3u}(1b_{1u} \rightarrow 2b_{3g}(d_{yz}))$
	16007		MCD				
6	17778	15500	abs	0.029	0.00	-0.23	${}^3\text{B}_{3g}(1a_g(d_{x^2-y^2}) \rightarrow 2b_{2g}(d_{xz}))$
	17835		MCD				
7	18983	20200	abs	0.012	0.001	-0.03	${}^3\text{B}_{2u}(1a_u \rightarrow 2b_{3g}(d_{yz}))$
	18726		MCD				

the TDDFT calculation three transitions having d–d origin are predicted at transition energies in reasonable agreement with the experiments (Table 10). The calculated oscillator strengths are, however, zero, but the transitions may borrow intensity from the near lying intense allowed transitions by low-symmetry distortions and vibronic coupling and spin–orbit coupling effects.

A TD-DFT calculation has also been performed for the free $[\text{Co}(\text{L})_2]^{1-}$ ion in a vacuum. The results are found to be similar to that of the calculated spectrum in CH_2Cl_2 solution and are compared in the Supporting Information Table S1.

The TD-DFT calculation thus leads to an acceptable agreement with the experimentally observed absorption spectrum of $[\text{Co}(\text{L})_2]^{1-}$. As expected for compounds of this class,^{37,43,44} the most intense transition arises from the $1b_{1u} \rightarrow 2b_{2g}$ transition (band 3) and mainly contributes to the observed blue color of the complex. However, it appears that the calculation underestimates the mixing of the intense and weak bands, thereby leading to too-low intensities for the weak and too-large intensities for the strong bands.

To put the results obtained for $[\text{Co}(\text{L})_2]^{1-}$ into perspective, calculations have also been performed on the corresponding $[\text{Fe}(\text{L})_2]^{2-}$ species. However, these calculations are more complicated since the total charge is -2 , which means that in vacuum calculations the highest occupied levels are already unbound, which causes problems in the excited-state calculations. Consequently, the calculated spectrum for $[\text{Fe}(\text{L})_2]^{2-}$ ion in a vacuum predicts two intraligand $n\pi^*$ transitions at 540 nm (oscillator strength (f_{osc}) = 0.01) and 437 nm (f_{osc} = 0.03), respectively, which are not observed in the experimental spectrum. It is thus essential to stabilize the negative charge through a dielectric continuum model, which was chosen to be the COSMO model²⁹ in the present study. In our implementation, the transition energies contain, apart from the altered “solvated” orbitals (slow term), also the contributions from the “fast” solvent response term.⁴⁵ The calculated spectrum for the same complex ion in CH_2Cl_2 solution is found to be in better agreement with the experiments. The abovementioned $n\pi^*$ transitions undergo a blue shift and are now calculated at 385

nm (f_{osc} = 0.03) and 365 nm (f_{osc} = 0.006), respectively. All the spin and electric dipole allowed transitions, occurring in the visible region for the cobalt species are, however, predicted to be at much higher energies in the iron case and do not appear among the first 25 states (5500–25 000 cm^{-1} range) in both the calculations, that is, are higher than 25 000 cm^{-1} in the calculation. Thus, the calculated spectrum for $[\text{Fe}(\text{L})_2]^{2-}$ does not contain any band of LMCT origin in the 22 000–10 000 cm^{-1} range, in agreement with the experimental data.

Summary

The DFT calculations reported in this article for the $[\text{Fe}(\text{L})_2]^{2-}$ and the $[\text{Co}(\text{L})_2]^{1-}$ species nicely reproduce the experimental trend of the very similar **D**-tensors and drastically different absorption spectra in the two cases. This is attributed to the differences in the nature of the transitions that contribute to the **D**-tensors and the absorption spectra. As explained before, the main contributions to the **D**-tensor come from the spin-conserving low-energy d–d excitations, which occur at comparable energies in the iron and the cobalt species, which in turn accounts for the similar *D* values in the two cases. While these transitions are observed in the case of the Co species, possibly due to intensity borrowing from the nearby intensely allowed transitions, they have not been observed for the iron species.

In general, the absorption spectra of such square-planar $[\text{M}(\text{L})_2]^z$ species are usually dominated by transitions that are either LMCT or LLCT in origin. In the present study, the observed differences in the electronic spectra of the $[\text{Co}(\text{L})_2]^{1-}$ and the $[\text{Fe}(\text{L})_2]^{2-}$ species are traced to the difference in the transition energy for the $1b_{1u} \rightarrow 2b_{2g}$ transition. For the former, this transition occurs in the visible and is strongly blue-shifted to the UV region in the latter. It is important to note that the same transition had been found to occur at very low energy ($\sim 8000 \text{ cm}^{-1}$) for the $[\text{Ni}(\text{L}_N)_2]^{1-}$ species.⁴⁴ This difference in the transition energy can be attributed to the difference in the metal contribution of the $2b_{2g}$ SOMO in the above three cases. As shown in Figure 9, the $2b_{2g}$ SOMO represents the π -superexchange interaction of the ligand b_{2g} combination with the metal d_{xz} orbital. Because this interaction is antibonding, it raises the energy of the $2b_{2g}$ orbital over the ligand $1b_{1u}$ orbital. In $[\text{Ni}(\text{L}_N)_2]^{1-}$, as explained in details in refs 37 and 44, the 3d orbitals are lying very low in energy owing to high Z_{eff} of

(43) Herebian, D.; Wieghardt, K.; Neese, F. *J. Am. Chem. Soc.* **2003**, *125*, 10997.(44) Herebian, D.; Bothe, E.; Neese, F.; Weyhermüller, T.; Wieghardt, K. *J. Am. Chem. Soc.* **2003**, *125*, 9116.(45) Klamt, A. *J. Phys. Chem.* **1996**, *100*, 3349.

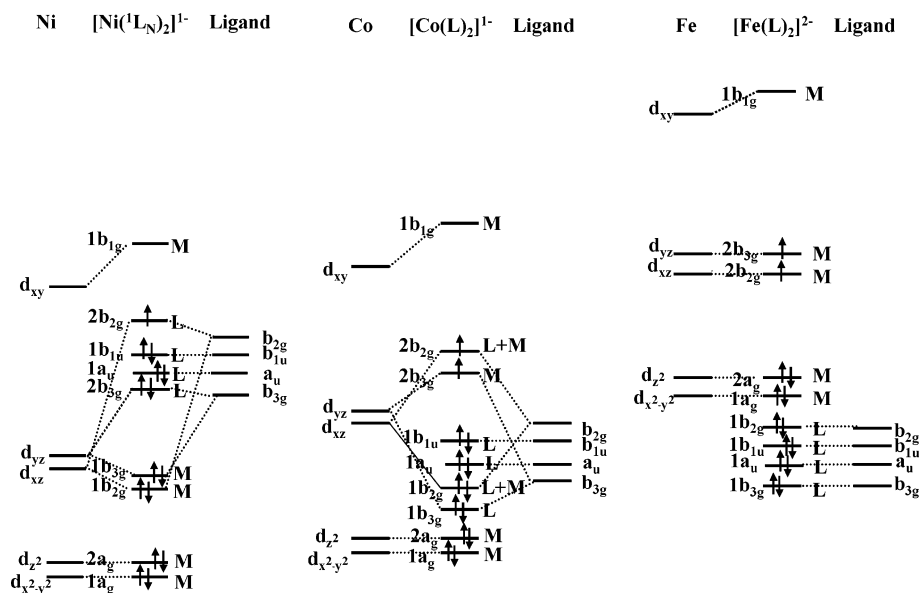


Figure 9. MO schemes of $[\text{Ni}^{\text{II}}(\text{L}_N^{\text{ISQ}})(\text{L}_N^{\text{IP}})]^{1-}$, $[\text{Co}(\text{L})_2]^{1-}$, and $[\text{Fe}^{\text{II}}(\text{L})_2]^{2-}$.

Ni and especially the $2b_{2g}$ level is predominantly of ligand character. Consequently, the $1b_{1u} \rightarrow 2b_{2g}$ (LLCT in origin) transition takes place at a very low energy (Figure 9).

The situation is just reversed in the $[\text{Fe}(\text{L})_2]^{2-}$ species. As explained earlier, the Fe 3d orbitals are situated very high in energy as compared to the ligand orbitals owing to low Z_{eff} of Fe. The $2b_{2g}$ orbital is predominantly metal in character (Figures 7 and 9). The $1b_{1u} \rightarrow 2b_{2g}$ transition is now LMCT in origin and takes place in the UV region.

Co^{II} has an effective nuclear charge between Ni^{II} and Fe^{II} .⁴⁶ Thus, in $[\text{Co}(\text{L})_2]^{1-}$ the Co 3d orbitals are placed such that they possess energies comparable to the ligand π^* orbital. As a result, there is considerable mixing of the metal and the ligand character in the $2b_{2g}$ level.³⁷ Thus, the $1b_{1u} \rightarrow 2b_{2g}$ transition contains both LMCT and LLCT contributions and is observed in the visible region.

Conclusions

In the present study, the electronic structures of two isoelectronic bis-dithiolato complexes $[\text{Fe}(\text{L})_2]^{2-}$ (**1**) and $[\text{Co}(\text{L}^{\text{Bu}})_2]^{1-}$ (**2**) were investigated in some detail experimentally and theoretically. The results establish that the electronic structures of the two species are very different. Compound **1** is best described as containing an intermediate-spin ferrous ion bound to two innocent dianionic dithiolene ligands. Such intermediate-spin ferrous species have a rather low effective nuclear charge. Consequently, the metal d-based orbitals are high in energy, and the charge transfer from the dithiolene ligands to the metal is limited in the electronic ground state. The situation is different for complex **2**, which formally contains a $\text{Co}(\text{III})$ ion with a much higher effective nuclear charge. This higher effective nuclear charge brings the metal d-based orbitals so far down in energy that they are at comparable energy with the highest ligand-based orbitals. Consequently, there is a large amount of ligand-to-metal charge transfer in the electronic ground state up to the point where the ligands can no longer be regarded as innocent and the actual electronic structure contains major

contributions from both $[\text{Co}^{\text{III}}(\text{L}^{2-})(\text{L}^{2-})]^{-}$ and $[\text{Co}^{\text{II}}(\text{L}^{2-})(\text{L}^{\bullet-})]^{-}$ resonance forms.

On the basis of this description, a detailed interpretation of the spectroscopic properties of the two compounds was developed. Particularly striking are the very large positive zero-field splittings of **1** ($D = +28 \text{ cm}^{-1}$) and **2** ($D = +32 \text{ cm}^{-1}$). The actual value for **2** has been measured independently by SQUID magnetometry, far-infrared absorption, and variable-temperature, variable-field magnetic circular dichroism spectroscopies. On the basis of a pilot density functional theory study of this property, the physical origin of the large ZFS is in both cases the presence of low-energy spin-allowed d–d excitations which lead to a large D_{zz} (normal to the plane of the complex) through efficient spin–orbit coupling. The value for the Co complex is a little higher since it has a large one-electron SOC constant ($\sim 600 \text{ cm}^{-1}$ for $\text{Co}(\text{III})$) versus $\sim 400 \text{ cm}^{-1}$ for $\text{Fe}(\text{II})$), which is, however, also more strongly covalently reduced for **2** compared to **1** such that the observed ZFS values are similar.

In addition to the calculated structures and ground-state properties, the calculations were also extended to the excited states of the systems studied, and the absorption and MCD spectra of **2** have been successfully interpreted. On the basis of these calculations, the absence of any strong absorption band in the visible region for **1** is, again, attributed to the energetic inaccessibility of the high-lying iron 3d-based orbitals which cannot act as acceptor orbitals in LMCT transitions. By contrast, the energetically low-lying cobalt d-based orbitals in **2** induce partial hole character in the ligands through extensive charge transfer. This opens the pathway for intense ligand-to-ligand charge transfer and also provides suitable acceptor orbitals for LMCT transitions that overall lead to rather rich optical spectra for **2**.

The present study thus demonstrates that dithiolato complexes can have a quite variable electronic structure leading to fascinating physical properties that can be efficiently probed through a combination of advanced spectroscopic and theoretical techniques.

Acknowledgment. J.v.S., F.N., and S.P. thank the Deutsche Forschungsgemeinschaft for financial support within the priority

(46) Shadle, S. E.; Hedman, B.; Hodgson, K. O.; Solomon, E. I. *J. Am. Chem. Soc.* **1995**, *117*, 2259.

program 1137 ("Molecular Magnetism"). We are grateful to the Fonds der Chemischen Industrie for financial support. K.R. gratefully acknowledges the Max-Planck Society for a stipend.

Supporting Information Available: Tables containing the results of the TD-DFT calculations in CH_2Cl_2 solution

(COSMO) and in a vacuum for the $[\text{Co}(\text{L})_2]^{1-}$ anion and X-ray crystallographic data for the complexes (PDF, CIF). This material is available free of charge via the Internet at <http://pubs.acs.org>.

JA042803I